Available online at www.sciencedirect.com
ScienceDirect
Composite Structures 85 (2008) 175–187
COMPOSITE STRUCTURES
www.elsevier.com/locate/compstruct

Interlaminar fatigue crack growth of cross-ply composites under thermal cycles

Narayanan Ramanujam [a], Pavankiran Vaddadi [a,1], Toshio Nakamura [a,*], Raman P. Singh [b]

[a] Department of Mechanical Engineering, State University of New York at Stony Brook, NY 11794, United States
[b] School of Mechanical and Aerospace Engineering, Okalahoma State University, Stillwater, OK 74078, United States

Available online 17 October 2007

Abstract

The fatigue growth of a fiber reinforced composite laminate was characterized under thermal cycling using a combined experimental and computational investigation. Twenty-four ply composite laminates ($[0^\circ_{12}/90^\circ_{12}]$) are fabricated with a pre-existing delamination, and subjected to thermal cycling in an environmental chamber. The large mismatch in the coefficients of thermal expansion is used to grow an interlaminar crack at the interface of the 0° and 90° laminae. This thermal fatigue crack growth behavior is investigated for different amplitudes of temperature change ($\Delta T = 30$–140 °C). The inspection of fracture surfaces, after completion of the fatigue tests, reveals an angled or kinked crack front growth with greater propagation distances near the free-surfaces/edges. Due to the non-uniform crack growth across the specimen thickness, three-dimensional finite element analyses are performed to investigate the fatigue growth mechanisms under thermal load. From the analysis, the energy release rate as well as the mixed-mode stress intensity factors is calculated and the variations of these fracture parameters are found to be consistent with the observed crack front configuration. Using the computed results, the experimentally measured crack growth rates are also correlated with the amplitude of energy release rate, and a power law form of the fatigue law is established. The relevant coefficients as well as the threshold energy release rate are also determined. The present analysis is useful for not only understanding the fatigue delamination mechanisms under thermal cycling but also for estimating the threshold temperature variation that is needed to drive crack growth.

Keywords: Mixed-mode fracture; Fracture toughness; Energy release rate; 3D finite element

1. Introduction

Fiber reinforced composites are commonly used as structural components in aerospace applications. In addition to designed mechanical or structural loads, they are often subjected to repeated temperature fluctuations during their service life. Since many composites are utilized in cross-ply arrangements, temperature changes can generate large internal thermal stresses. Typically, the difference in the coefficients of thermal expansion (CTE) along 0° and 90° directions exceeds $30 \times 10^{-6}/^\circ$C which can produce thermal stresses of 20 MPa or more under $\Delta T = 100$ °C. Furthermore, other environmental conditions such as moisture may also cause mismatched expansions and generate additional stresses within composite laminates. At the microscale, hygrothermal stresses also arise from mismatch in properties between fibers and the matrix [1]. These stresses, at various length scales, can generate matrix cracking and promote lamina delamination under thermal cycling.

Fatigue crack growth is one of the major failure mechanisms in composites [2–6]. The fracture process of composite laminates subjected to fatigue loading involves a sequential accumulation of intra- and interlaminar damage in the form of transverse cracking, fiber splitting and delamination prior to catastrophic failure [7]. Fatigue of composite materials can be driven by mechanical loads, thermal loads or a combination of both [5], and several empirical models have been proposed to analyze fatigue

* Corresponding author. Tel.: +1 631 632 8312; fax: +1 631 632 8544.
E-mail address: toshio.nakamura@sunysb.edu (T. Nakamura).
[1] Present address: Currently at State University of New York at Farmingdale, NY 11735, United States.

0263-8223/$ - see front matter © 2007 Elsevier Ltd. All rights reserved.
doi:10.1016/j.compstruct.2007.10.018

behavior. Eselun et al. [8] noted influences of resin microcracks, generated by thermal cycling, on fatigue life, tensile strength and interlaminar shear strength. Cohen et al. [9] found that during thermal cycling, cracks accumulated up to a brief number of cycles, remained constant, and later increased. Herakovich and Hyer [10] studied thermal cycling crack density as a function of layer thickness and number of transverse plies. They also found extensive damage in epoxy resin that included delamination. Adams et al. [11] showed the effects of space environment on cross-ply composites and concluded that cracks tend to avoid resin rich areas and delaminations grew from transverse cracks. Others reported that elastic properties of thermally cycled carbon fiber composites were not significantly reduced while transverse tensile strength and interlaminar strength were appreciably reduced [12,13]. Another study characterized crack growth in epoxy due to thermal fatigue [14]. Here, the fracture specimen was a composite disk consisting of outer ring of epoxy bonded to an inner invar plate. The growth rate of radial cracks was correlated with energy release rate from finite element analysis. Many of these studies assumed the crack density as a function of thermal cycles.

Investigations on interlaminar delamination growth due to thermal loading are rather limited. The effects of mechanical and thermal loads on fatigue were studied for curved layered composites by Figiel and Kaminski [5]. They used the linear elastic fracture theory and the finite element analysis to solve the fatigue delamination problem. Although not for composite laminates, Gurumurthy et al. [15] developed an experimental procedure for measuring the crack growth along polymer interfaces under hygrothermal fatigue. The experimentally measured crack growth per unit temperature cycle (da/dN) was correlated to the magnitude of the energy release rate ($\Delta\mathscr{G}$) during temperature cycles.

The current study is undertaken to elucidate the fatigue delamination growth under thermal load. Specifically, it reveals how an existing interlaminar delamination can propagate from temperature change without any external mechanical load. Following the thermal cycling tests, fatigued surfaces are closely examined to determine the fracture mode. In addition the rate of crack growth is correlated with the range of energy release rate (obtained via computational models) using both 2D and 3D models. The relation is used to determine the level of threshold energy release rate needed to sustain crack growth phenomenon.

2. Experimental procedure

2.1. Specimen preparation

Carbon fiber reinforced epoxy composite laminates were prepared using vacuum bagging with unidirectional carbon fiber cloth C383 (acquired from CST Sales, Tehachapi, CA). The fiber cloth was smooth webbed having a weight of 133.2 g, width of 305 mm and thickness of 0.152 mm. As a part of the epoxy system, Epon 862 resin, a low viscosity, liquid epoxy resin manufactured from epichlorohydrin and Bisphenol-F was used (Hexion Speciality Chemicals, Houston, TX). This system offers several advantages like long working life, high elongation, and is a very versatile processing system for fabricating fiber reinforced pipes, tanks and composite parts. In order to cure the epoxy a curing agent, Epi-cure was used by 15% of the weight of resin. Finally, the specimen was post-cured for 2 h at 120 °C.

The vacuum bagging procedure was use to fabricate $[0^\circ_{12}/90^\circ_{12}]$ laminates consisting of twelve 0° and twelve 90° plies. This unique arrangement was chosen to maximize the stresses generated by the thermal expansion mismatch between 0° and 90° plies. Nonetheless, as expected, such an unsymmetrical lay-up also caused slight warping of the composite plate, especially towards the edges. To minimize the effects of curvature, test specimens were cut from relatively flat, central portion of plate. It should be noted that, for the current model, the effects of curvature and residual stresses should be minimal since it is the cyclic amplitude, and not the absolute values of stresses, that controls the fatigue growth behavior. In addition, to quantify the effects of unsymmetrical lay-up, the crack driving forces (e.g., energy release rate) were also computed with more common symmetrical arrangements. This is reported in Section 4.

Prior to curing, a pre-existing delamination crack was introduced along this interface by inserting a strip of Teflon tape. Test specimens were machined from the post-cured laminate using a water-cooled high-speed diamond saw, and then the edges were polished using 120, 400 and 600 grit metallographic papers to remove any microstructural damage that might have occurred during cutting. A schematic of the specimen configuration is shown in Fig. 1. Prior to thermal cycling, the crack faces were tapped to open to ensure no local bonding occurred (from residual epoxy) between the crack faces.

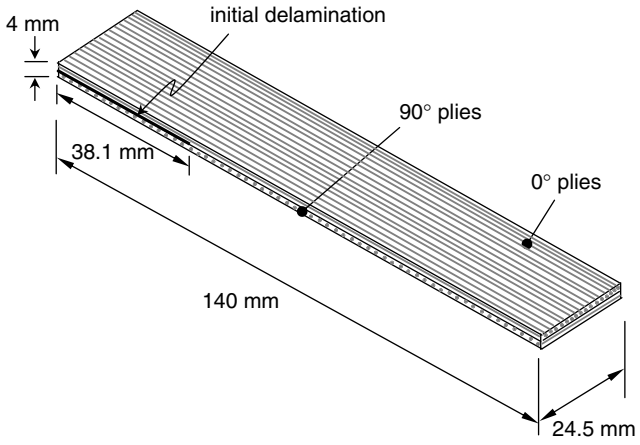

Fig. 1. Schematic of composite laminate with pre-existing delamination.

2.2. Mechanical and thermal properties of lamina

Our primary goals are to characterize crack growth in composites under thermal cycling and to investigate if the growth rate follows the Paris-law, as for fatigue under mechanical loading [16]. The latter analysis requires the estimation of fracture parameters, as well as mechanical and thermal properties of the composite material. To this end, separate specimens consisting of an 8-ply unidirectional laminate were fabricated using the same vacuum bagging process. Tensile tests were performed on these specimens to obtain load-displacement data as well as independent strain measurements from gages bonded on the specimen surface. From tests conducted on both $[0_8]$ and $[90_8]$ specimens the tensile moduli in the longitudinal and transverse directions were measured to be $E_L = 105 \pm 2$ GPa and $E_T = 5.5 \pm 0.08$ GPa, respectively. Using the longitudinal modulus and known properties of the fibers and matrix, the fiber volume fraction was estimated to be 44% via the rule of mixtures. The estimated values of other mechanical parameters for the transversely isotropic materials were $\nu_{LT} = 0.33$, $\nu_{TT} = 0.30$ and $\mathscr{G}_{LT} = 3.50$ GPa. In order to estimate the poisons ratios, strain gages were bonded in both longitudinal and transverse directions to record the longitudinal and lateral strains.

The coefficients of thermal expansion (CTE) were determined by strain measurements on unidirectional laminates that were heated in an environmental chamber (Benchmaster BTRS, Lunaire Ltd., Williamsport, PA). Here the temperature was varied from 25 °C to 125 °C and strains were measured for unidirectional $[0]_8$ and $[90]_8$ laminates. To ensure accuracy, a separate aluminum plate with strain gages was placed in the same chamber to obtain reference strain measurements. During the experiment, the temperature was raised at 20 °C intervals, and the system was allowed to stabilize for few minutes to ensure thermal equilibrium. The accuracy of the strain measurements was further verified subsequently by raising the temperatures directly to intermediate values and comparing strains with earlier measurements. The measured CTE exhibited slight temperature dependence. However, since it was not significant, the temperature variation was not considered and the average value was chosen for the present analysis. The longitudinal and transverse coefficients were estimated to be $\alpha_L = 0.63 \times 10^{-6}$ °C and $\alpha_T = 32 \times 10^{-6}$ °C, respectively. The procedure for determining these coefficients are discussed in further detail in another work [17]. Here, from strain variation of composite laminate with temperature, the CTE of epoxy was estimated through an inverse analysis procedure. However, since information on CTE of fiber is well documented, this value was treated as known.

Prior to the thermal fatigue tests, similar pre-cracked specimens were utilized to estimate fracture resistance under monotonic mechanical load. Using the double cantilever beam set-up with attached hinges at the ends, the specimen was fractured under opening mode. The measured toughness was $\mathscr{G}_{Ic} = 155 \pm 7$ J/m^2. The specimen was also loaded under 4-point-bend to generate shear dominated mode. However, the specimen failed at the surface of 90° ply before the crack growth initiation could occur along the interlayer.

2.3. Thermal cycling

Thermal cyclic loading tests were conducted using the same environmental chamber used to measure CTE. It provides automated cyclic or constant condition at certain temperature as well as humidity. In the current experiments, in order to minimize any effects of moisture absorption, the relative humidity was set at ~0%. The objective of the thermal cycling tests was twofold, first to measure the crack growth length as a function of the number of thermal cycles, and second to observe the effect of temperature range on the crack growth rate. Accordingly, different ranges of temperatures were employed. A typical thermal cycle was carried out as follows. In the case of $\Delta T = 140$ °C, initially the temperature was maintained at 20 °C for 10 min. This was followed by a steady ramp up to 160 °C within 30 min. Then the temperature was held constant at 160 °C for 30 min to ensure thermal equilibrium throughout the specimen. Finally the specimen was cooled down to 20 °C in 40 min. The entire thermal cycle lasts about 110 min.

Measurements of the crack length were made after every twenty thermal cycles with simple visual crack detection after the specimen surfaces were masked by white correction tape to highlight the location of current crack tip. These measurements were made for two separate specimens under an optical microscope at a magnification of 50 times the original size. In order to determine the length, an image of a micro-scale with a precision of 10 μm was superimposed on the picture. Two separate specimens were used in the measurement. For each specimen, the crack tip positions on both sides were measured. In this manner the crack length was established as a function of the number of thermal cycles.

Fig. 2 shows the optical micrographs of crack growths after different numbers of thermal cycles. For each measurement, the specimen was taken out of the environmental chamber for about 8 min, which is presumed to be short enough to have minimal effects on the crack growth behavior. The crack growth behavior is shown as a function of thermal cycle in Fig. 3a. Here the average of 4 measurements is plotted for up to 920 cycles or about 70 days. Note that the variations of crack lengths were generally within ±2% among the four locations. However, it is important to note that these measurements were made at the surfaces and they do not necessarily represent the crack length through the thickness. Uneven or curved through-thickness crack growth is discussed later in Section 2.4. During the test, the temperature amplitudes were varied as indicated in the Fig. 3. The initial amplitude of $\Delta T = 140$ °C was intentionally chosen to be large to ensure crack initiation

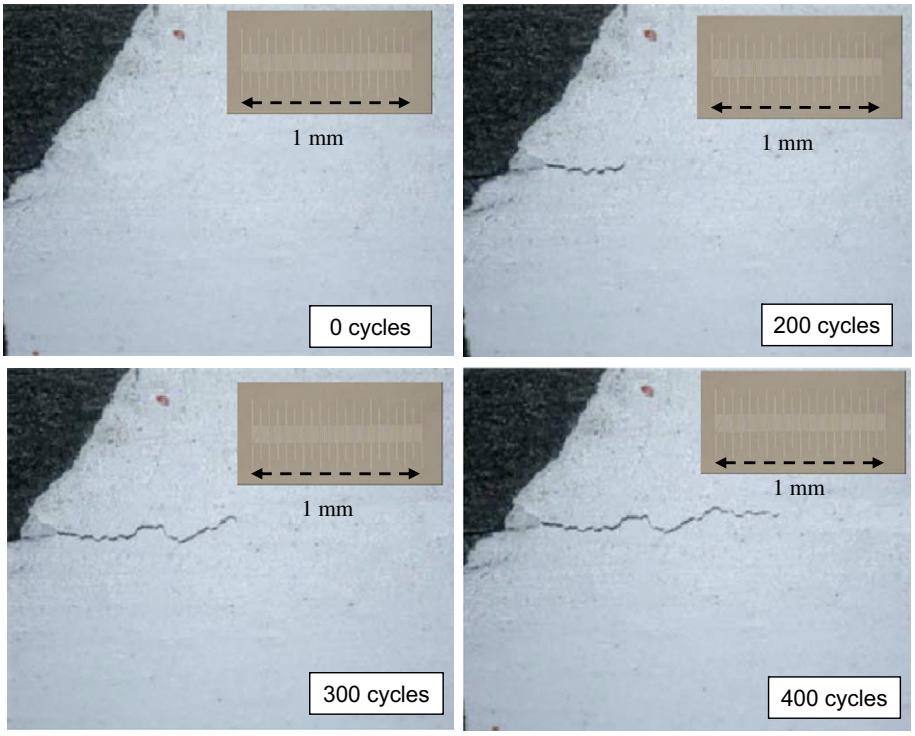

Fig. 2. Optical micrographs showing crack growth along the interface between the 0° and 90° plies at different thermal cycles. Specimen is masked with white tape to show crack better.

and growth. The four subsequent temperature amplitudes of $\Delta T = 60$ °C, 30 °C, 100 °C, and 120 °C were prescribed during the measurement period to systematically vary the crack growth behavior. Since the temperature amplitudes needed to drive the crack at various rates were not known a priori, they were determined by trial-and-error during the course of the experiment. In Fig. 3a, the slope represents the crack growth rate for given temperature amplitudes. Fig. 3b shows the crack growth rate per cycle.

The effects of temperature amplitude can be clearly observed in these figures. During the initial phase of $\Delta T = 140$ °C, it took about 240 cycles to reach steady state propagation when the growth rate was estimated to be $da/dN = 5.1$ μm/cycle. At 500th cycle, the temperature amplitude was switched to 60 °C and maintained for 100 cycles. The smaller number of cycles was chosen since it was observed that the propagation reached steady state much faster. Nonetheless, the steady state rate of crack was lowered. In the subsequent phase (after 600 cycles), ΔT was further reduced to 30 °C. With this temperature variation, the measurements showed no visible change in the crack length even after 80 cycles. It is likely that driving force to fatigue growth is below the threshold value. Note that prior to testing, we had no knowledge of the dependence of ΔT on the delamination growth. Thus the temperature changes were assigned based on the crack growth behavior observed in the previous segment. The next ΔT was chosen to be 100 °C. As the measurements were made, it took longer time to reach steady state. This is probably because the crack was arrested for about 6 days at $\Delta T = 30$ °C and some healing might have occurred near the crack tip. To ensure steady state condition the $\Delta T = 100$ °C condition was maintained for 180 cycles. For the final test, the temperature amplitude was set at $\Delta T = 120$ °C for 60 cycles. Although a detailed analysis was not carried out to determine dependence on loading history (i.e., order of imposed ΔT), such an effect is likely to be minimal for crack growth after steady state has been reached.

2.4. Fracture surfaces

The fracture surfaces were examined at the conclusion of the thermal cycling test. To open the crack surfaces for microscopy the specimens were immersed in a nitrogen bath and then split in half along the crack plane. Fig. 4 shows optical and SEM micrographs of the fracture surfaces which revealed unexpected crack growth phenomena. Two specimens showed non-uniform propagation across the thickness or crack front, and the cracks appeared to grow from the edge or free-surface toward the interior. At the mid-section, there was essentially no propagation. Also, the propagation behavior was nearly symmetric about the mid-point. The average angle between the initial crack front and the kinked crack front was measured to be 43.5°.

The micrographs also showed three different exposed surfaces belonging to the 0° and 90° fiber layers and the interlaminar epoxy phase. This observation suggests non-planar growth of the crack front during the fatigue process. A closer inspection on the non-planar crack surface was

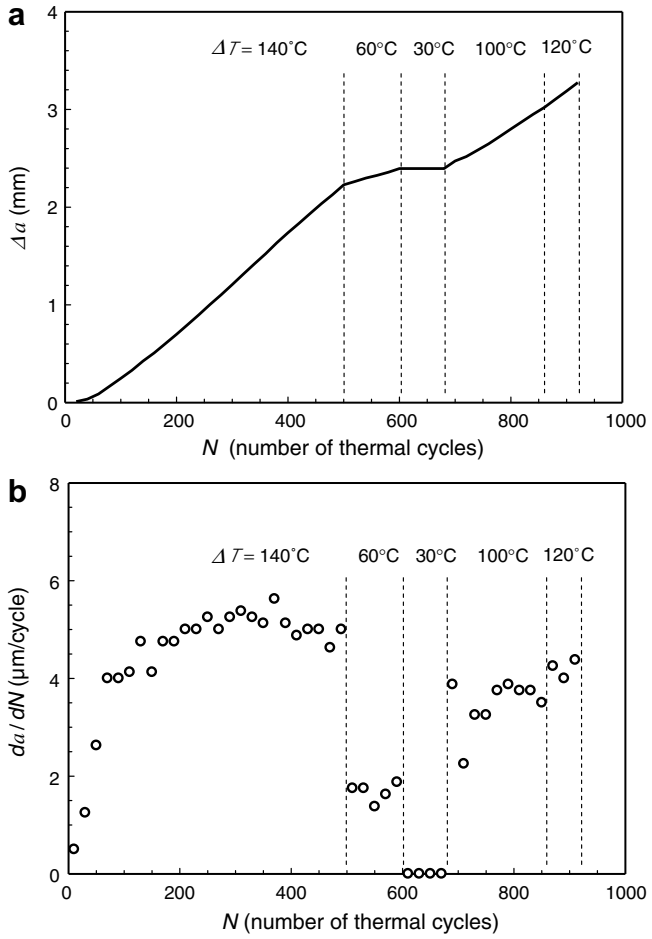

Fig. 3. (a) Average crack length measured at edges shown as a function of thermal cycles. (b) Average growth rate under different amplitude of thermal cycles.

made using an optical surface profiler (Digital Microscope, Keyence, VHX-500K, Osaka, Japan). Fig. 5a shows the topology of the crack surface near the line denoted as *A–B* in Fig. 4. The zero depth was set to the middle of interlaminar epoxy phase which in turn was measured to be 15 μm thick using optical microscopy of the specimen edge. The measured depth variation between the points *A* and *B* is also shown in Fig. 5b. Here three different phases are superimposed to show approximate location of crack. The crack is initially located within the 0° ply, designated as point *A*. The crack then enters into the epoxy phase before finally entering the 90° ply. Similar alternating crack planes were also observed for the other specimen whose micrograph is not shown here.

The observed nonlinear crack plane suggests that the interlaminar epoxy layer is sufficiently tough so as to not represent a weak plane. Otherwise the crack would have most likely chosen a weak plane to propagate. Crack growth in alternating planes is also driven by the predominantly Mode II condition, as described in the next section. The large shear condition coupled with the crack contact condition may generate the unstable crack growth condition. In addition, although not determined in this analysis, the *T*-stress might have also played a role. These observations of fracture surface dictate the necessity for a 3D model to analyze fatigue growth behavior. The following section describes the computational procedure used to determine the energy release rate as well as the mixed-mode stress intensity factors.

3. Computational analysis of 3D thermal crack

3.1. Finite element models

Since no analytical solutions exist for a three-dimensional crack front in a composite laminate, a finite element model was constructed to identify the relationship between thermal loading and the fracture parameters. Three crack front configurations were considered for analyses. Two of these include the initial straight crack front (before propagation) and the final angled or kinked crack front (after propagation) shown in Fig. 4. In between, an additional model was also generated based on estimated crack front evolution during thermal cycling process. For homogenous materials, Heyder and Kuhn [18] utilized transparent materials to record evolution of crack front in their 3D fatigue crack propagation study. Similar observations of the growing crack front would have been ideal even in this case. Nonetheless, this is not possible due to the opaque nature of the specimen. Furthermore, carrying out a series of interrupted tests would require a very large number of specimens and a prohibitively lengthy test period.

To construct the final crack front configuration, dimensions of fracture surfaces of two specimens were measured. As described in the previous section, the crack front consists of three nearly linear sections. One at the middle and two inclined at the sides with the kink angle being 43.5°. A schematic of delamination model is shown in Fig. 6. Since intermediate crack front shapes were not known, we assumed them to maintain the similar angle between the middle crack front and the angled crack front. Although other growth models are possible, all should have similar fracture parameter variations (e.g., energy release rate along crack front), at least qualitatively. In this study, three separate models representing different stages of crack growth were constructed, as shown in Fig. 6. The first model (crack front *A*) is for the initial stage possessing a straight crack front along the width direction (the configuration prior to thermal cycling). Next model corresponds to an intermediate stage of crack propagation (crack front *B*). A third model (crack front *C*) represents the measured growth at the final stage. In addition, the crack growth was assumed to be planar even though vertically alternating crack paths were observed, as shown in Fig. 5. Although such a behavior is also an important subject of interlaminar crack growth, the study would require detailed microstructural models. Since our present aim is to understand the fatigue growth behavior at continuum level, our 3D models did not take into account the non-planar growth.

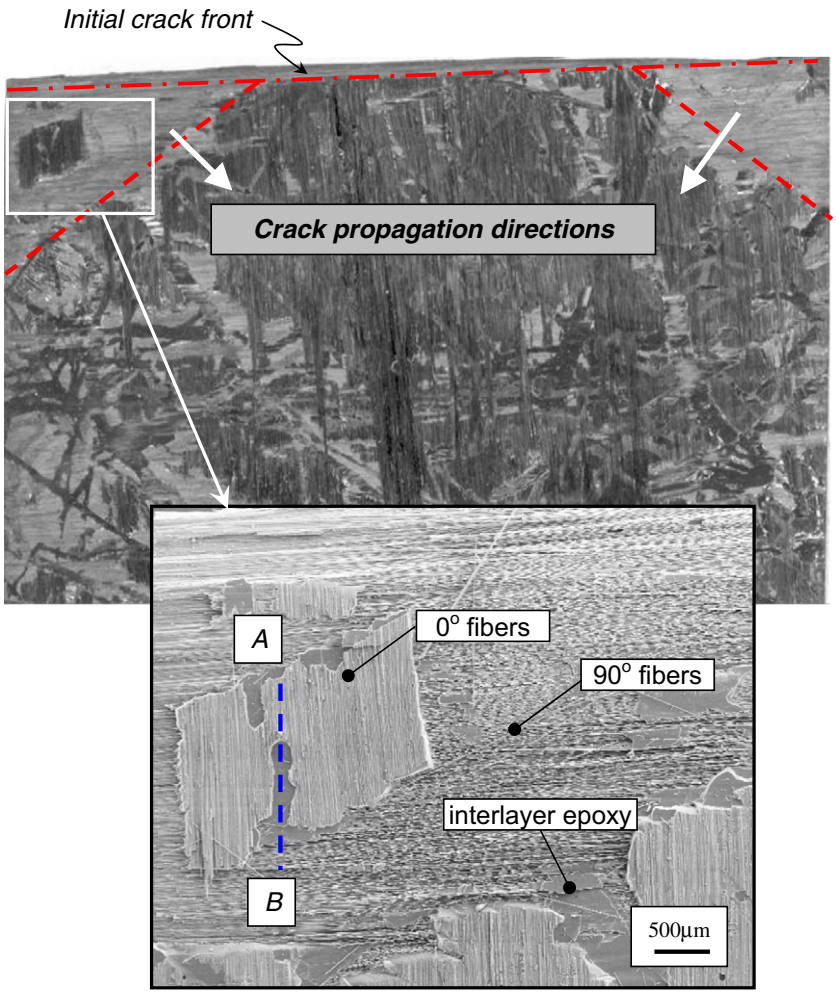

Fig. 4. Optical and SEM micrographs showing fractured surface. Estimated crack propagations are indicated. Note the surface exposes fibers in both directions as shown in the enlarged micrograph.

In order to construct the finite element model, a mesh generator was developed. The symmetry condition was utilized to model only a half of the actual specimens, fine elements were used at the crack front, and 30 element layers were taken along the half-width of the specimen. A selectively refined mesh was used to ensure accurate computations of mixed-mode stress intensity factors along the crack front. The final crack growth configuration model, shown in Fig. 7, contains approximately 60,000 eight-noded brick elements. The material model was chosen to be transversely isotropic and the properties reported in Section 2.2 were assigned. The upper half was modeled as 0° ply (fibers in the direction of crack growth) while the bottom half was modeled as 90° ply (fibers perpendicular to the direction of crack growth). During trial computations, a limited overlapping of top and bottom crack surfaces was observed (due to large Mode II condition). In order to circumvent the problem, contact conditions were enforced between the fracture faces to avoid overlapping. Furthermore, in order to minimize calculation errors for fracture parameters, the angled crack location was slightly smoothed by introducing a narrow transitional region that was 1.7 mm wide.

3.2. 3D fracture parameters

Using the 3D model, relevant fracture parameters along crack front were computed. For the orthotropic materials, the relationship between the energy release rate and three stress intensity factors is given as [19],

$$\mathscr{G} = \frac{H_A}{4\cosh^2(\pi\varepsilon)}|\boldsymbol{K}|^2 + \frac{H_B}{8}K_{\mathrm{III}}^2 \tag{1}$$

Here $\boldsymbol{K}$ is the complex stress intensity factor and is given by $\boldsymbol{K} = K_{\mathrm{I}} + \mathrm{i}K_{\mathrm{II}}$. Also the material constants H_A and H_B can be determined from the Hermitian matrix $\boldsymbol{H}$ and ε is the oscillatory index which depend on material properties. Note that $\boldsymbol{H}$ has a complex form for orthotropic bimaterials but H_A and H_B reduce to $4/E_{\mathrm{eff}}$ and $4/\mu_{\mathrm{eff}}$, respectively, for isotropic bimaterials in which case E_{eff} and μ_{eff} are the effective tensile and shear moduli. The determination of these parameters was shown by Nakamura et al. [19] and Yang et al. [20]. In the present model, they are $H_A = 0.5786$ GPa, $H_B = 1.399$ GPa and $\varepsilon = -0.0601$. Many experimental studies have shown that the critical energy release rate $\mathscr{G}_{\mathrm{c}}$ depends on the mode of fracture. Gen-

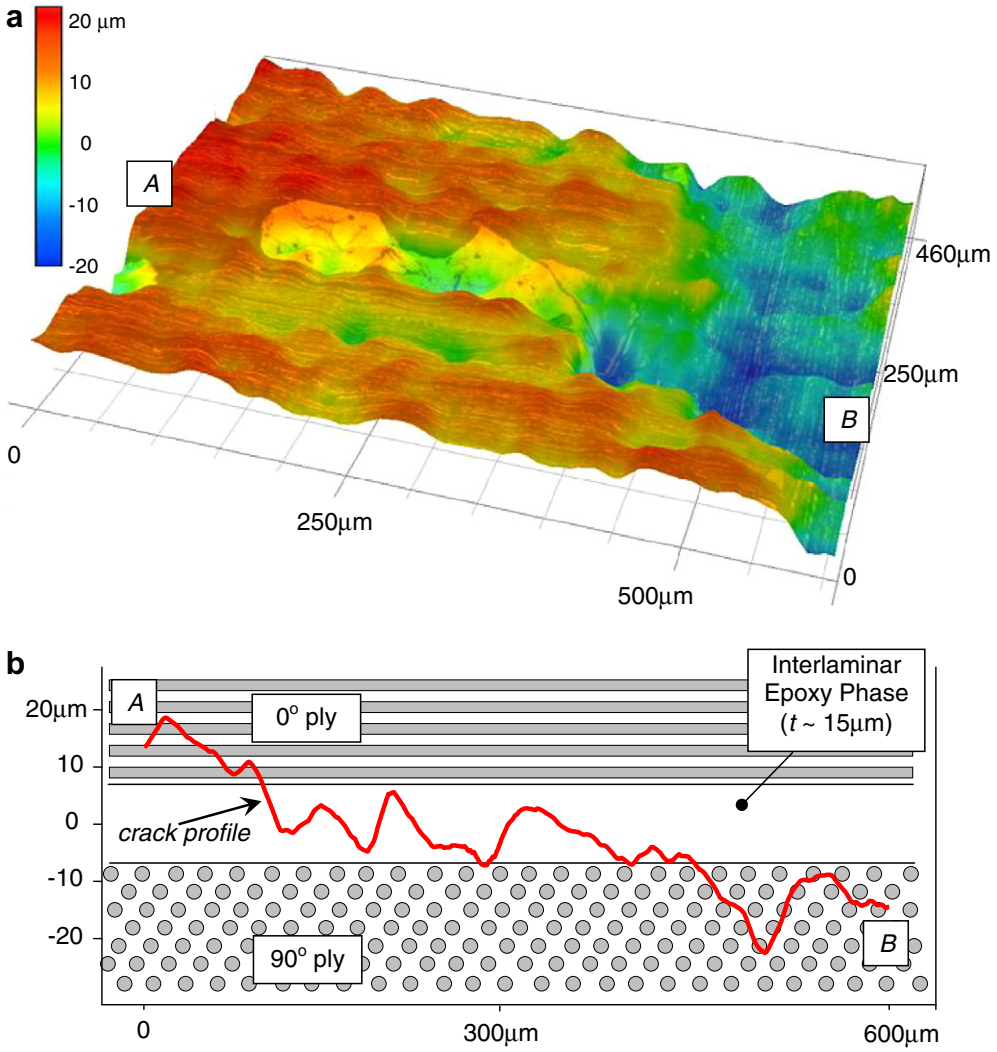

Fig. 5. (a) 3D fractured surface profile measured by Keyence profile microscope near line *A–B* in Fig. 4. (b) Measured crack profile between line *A–B*. Profiles of different phases are imposed on the graph.

erally under a predominantly Mode II condition, $\mathcal{G}_c$ is a few times greater than that under Mode I condition [21]. Thus, it is essential to quantify the mixed-mode state. A convenient way to define the mixed-mode condition is to use phase angles. For 3D cracks that can possess all three modes, it is necessary to utilize two phase angles, ψ and ϕ. The first phase angle must be defined in terms of a characteristics length scale, L, as,

$$\psi(L) = \tan^{-1}\left\{\frac{\mathrm{Im}(KL^{i\varepsilon})}{\mathrm{Re}(KL^{i\varepsilon})}\right\} \cong \tan^{-1}\left[\left(\frac{\sigma_{12}}{\eta\sigma_{22}}\right)_{r=L}\right] \tag{2}$$

where η is a traction resolution factor and given by $\eta = \sqrt{H_{22}/H_{11}} = 1.25$ in the current model. In our analysis, we have chosen $L = 80$ μm since the size of fracture process zone is probably about this length scale. However, a phase angle with other L may be obtained through the equation below

$$\psi(L_2) = \psi(L_1) + \ln\left(\frac{L_2}{L_1}\right) \tag{3}$$

The other phase angle that is related to the out-of-plane shear mode may be introduced as,

$$\phi = \cos^{-1}\left[K_{\mathrm{III}} \Big/ \sqrt{\frac{2H_A}{\cosh^2(\pi\varepsilon)H_B}\left(K_{\mathrm{I}}^2 + K_{\mathrm{II}}^2\right) + K_{\mathrm{III}}^2}\right] \tag{4}$$

In the present model where the crack front propagation is not linear, the magnitudes of two shear modes K_{II} and K_{III} depends greatly on the growth angle. Thus, it is useful to quantify the effective shear mode with respect to tensile mode, and an additional phase angle may be introduced as

$$\varphi = \cos^{-1}|\cos\psi\sin\phi| \tag{5}$$

Under pure Mode I conditions $\varphi = 0°$, and if the crack growth is dominated by shear then $\varphi \to 90°$.

3.3. Computed results

The three models shown in Fig. 6 were loaded by assigning a temperature increase at every node. The computed

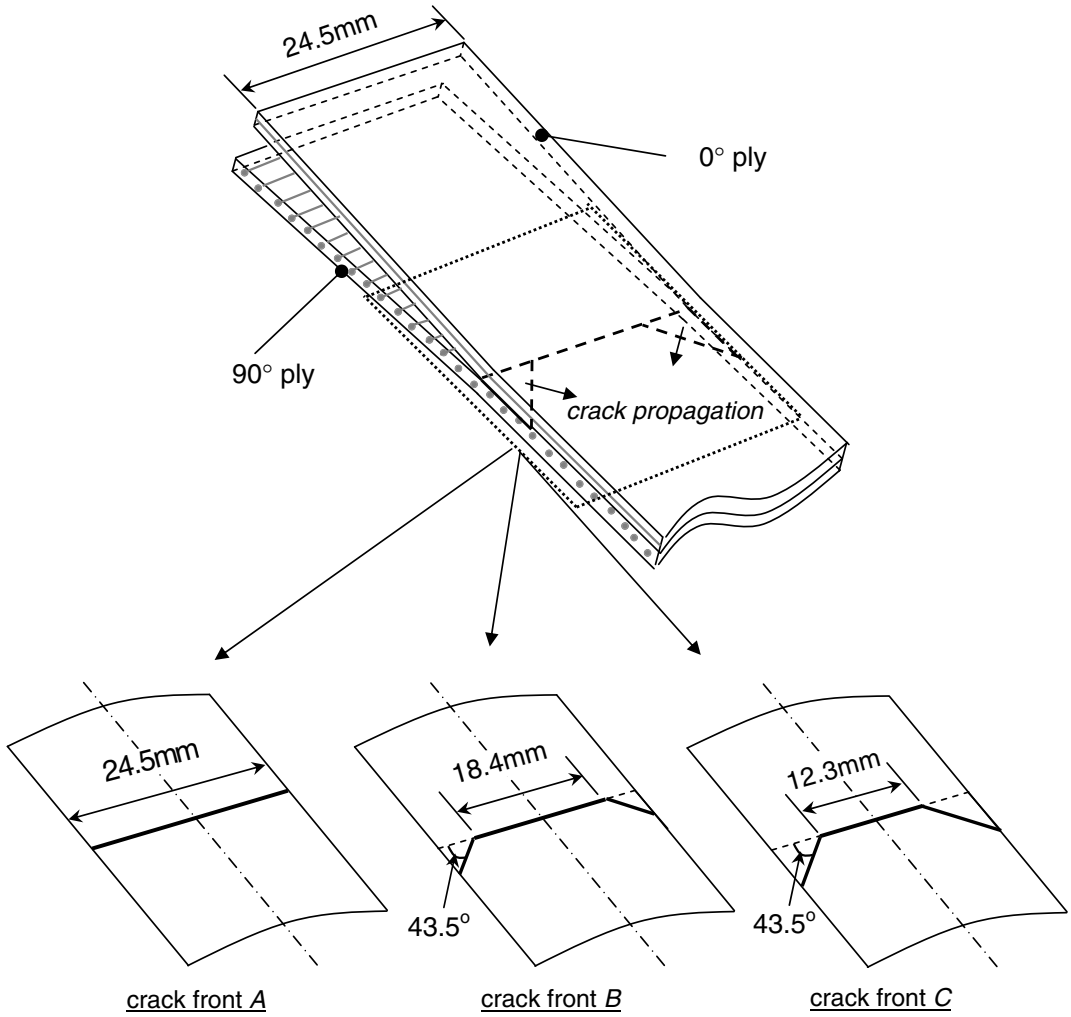

Fig. 6. Schematics of a section of the composite model, and three different crack configurations analyzed. Initial stage (crack front A), intermediate stage (crack front B) and final stage (crack front C).

effective stress contours near the crack fronts of model C under $\Delta T = 140$ °C are shown in Fig. 8. Two plots below shows the stress contours on the plane of crack on both sides, i.e., bottom 90° ply and top 0° ply. Note that the near front stresses exceed 150 MPa under this temperature. The high stresses indicated by red essentially denote the shape of kinked crack front. Large stresses can be also observed near the free-surface of uncracked ligament.

Fig. 9 shows the contours for different components of stress but only on the side of the 0° ply. The large tensile stress σ_{11} in the uncracked ligament corresponds to smaller CTE of the 0° ply. On the 90° ply, σ_{11} is negative at the uncracked ligament due to its larger CTE. The opening stress σ_{22} is not zero on the cracked surface but slightly negative. This indicates that crack surfaces are in contact and it is consistent with negative K_{I} results, as discussed next. The two shear stress components σ_{12} and σ_{23} show very large magnitudes ahead of crack front. The 3D energy release rates, computed via the domain integral [19], are shown as a function of the arc length measured from the center or symmetry plane in Fig. 10. Here the energy release rate is normalized by $hE^*(\Delta\alpha\Delta T)^2$, where h is the laminate thickness, E^* is the effective in-plane tensile modulus defined as $E^* = 4\cosh^2(\pi\varepsilon)/H_A$, and $\Delta\alpha = \alpha_{\mathrm{T}} - \alpha_{\mathrm{L}}$. The energy release rate for the crack front A shows a steep increase near the edge or the free-surface. Such behavior is consistent with a 3D interface crack under dominant Mode II condition [22]. Furthermore, it supports that the initiation point of crack growth is at the free edge, as observed on the fracture surfaces. For the other two models, the largest $\mathscr{G}$ occurs near the angled or kinked region as indicated in Fig. 10. It is also interesting to note that the location of maximum $\mathscr{G}$ shifts toward the mid-point as shown in the mid-stage model B and the final stage model C. In addition, the energy release rate is more even across the entire crack fronts in these models. In Fig. 10, the energy release from the plane strain model $(\mathscr{G}/hE^*(\Delta\alpha\Delta T)^2 = 0.112)$ is also indicated. This value is lower than any of 3D values due to greater constraint condition.

Due to the nature of thermal loading, the primary mode of crack growth was expected to be Mode II. The first

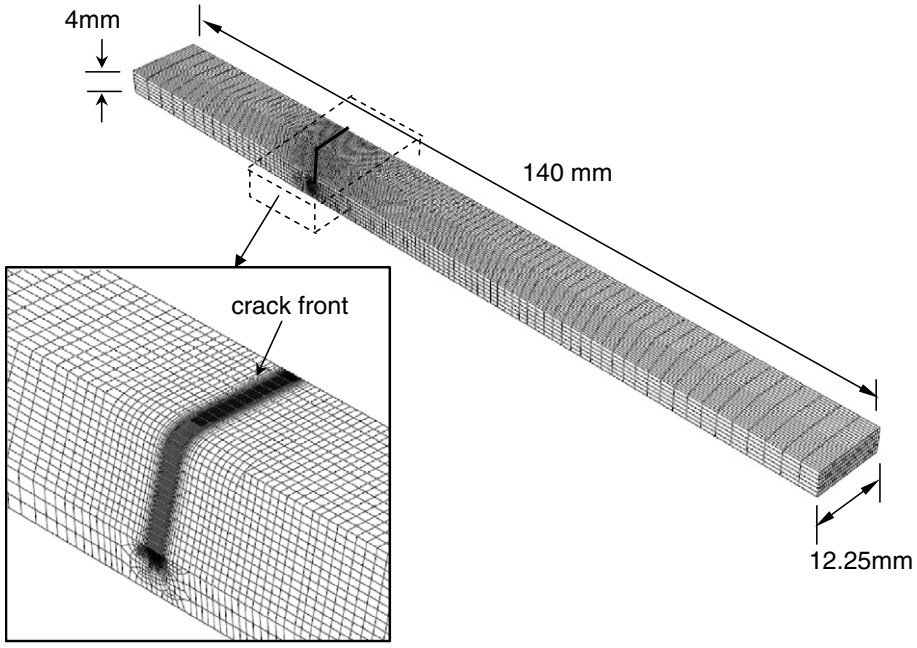

Fig. 7. 3D finite element mesh for crank front C model. An enlarged section of 90° ply (lower layer) exposing the crack front region is also shown.

phase angle ψ is shown in Fig. 11a. In all models, it is nearly constant at $\psi \cong 100°$ along the initial (unkinked) crack fronts. Note the sign of K_I is negative while K_{II} is positive with that angle. For the two angled crack front models (B and C), this angle suddenly changes beyond the transition region. In fact the sign K_{II} changes from positive to negative (at $\psi = 180°$). This occurs due to the shifting of crack propagation direction. The relative magnitude of K_{III} is shown via the second phase angle in Fig. 11b. Here at the mid-plane, $\phi = 90°$ due to the symmetry condition. In all cases, relative K_{III} increases toward the free-surface. For the crack front B and C models, a nearly pure Mode III condition (i.e., $\phi = 0°$) is observed near the transition region. These results are consistent with the shear stress contours shown in Fig. 9.

The combined effects of Modes II and III can be shown with the additional phase angle φ, as defined in (5). The variations of φ across the crack fronts are shown in Fig. 12. Here, regardless of the crack front shapes, the results are nearly identical for all models. In fact the value is always $80° < \varphi < 90°$ even along the kinked front except near the free-surface. These results essentially confirm that the shear mode is dominant throughout the crack fronts. Based on the results from the computational model and the observed crack front shape, it is likely that the delamination begins at the corner/free-surface and progresses at an inclined angle as depicted in Fig. 6. Using these results, the relationship between the fatigue growth rate and the thermal cycle is described next.

4. Fatigue crack growth characterization

As in homogeneous materials, the threshold resistance for fatigue crack growth in a composite material is expected to be less that under monotonic loading. Here we inspect the fatigue crack growth rate (da/dN) to determine the remaining life or an inspection interval of component. Based on the observed crack growth during thermal cycling and the relationship between the energy release rate and temperature change, the rate of fatigue growth is characterized. Since the local $\mathcal{G}$ is not uniform over the inclined or growing portion of the crack front, the average value was chosen from the results of crack front model C shown in Fig. 10. This value is $\mathcal{G}_{ave}/hE^*(\Delta\alpha\Delta T)^2 = 0.20$. Also since the actual crack growth is directed inward as well, the true growth rate is determined by multiplying the measured crack growth at free-surface by $\cos 43.5°$. The results are listed in Table 1.

In order to gauge the three-dimensional effects, a separate interpretation based on a 2D model was also made and is listed in the same table. Since the actual 3D crack growth shape cannot be determined, such an apparent relation based on a 2D interpretation should be useful in evaluating thermal fatigue growth.

Since a power law equation based on the Paris-law is a most common approach to relate the crack driving force and the growth rate, the following formula is considered

$$\frac{da}{dN} = C(\Delta\mathcal{G} - \Delta\mathcal{G}_{th})^m \tag{6}$$

Here C and n are material constants, and $\Delta\mathcal{G}_{th}$ is the threshold fatigue crack growth toughness. These parameters were obtained using a curve fitting program, and with 3D interpretation, they are, $C = 0.482 \times 10^{-6}$ [m/cycle (J/m^2)], $m = 0.44$ and $\Delta\mathcal{G}_{th} = 12.5$ J/m^2 (or $\Delta K = 0.30$ MPa $\sqrt{\text{m}}$) With 2D interpretation, they were $C = 0.869 \times 10^{-6}$ [m/cycle (J/m^2)^m], $m = 0.44$ and

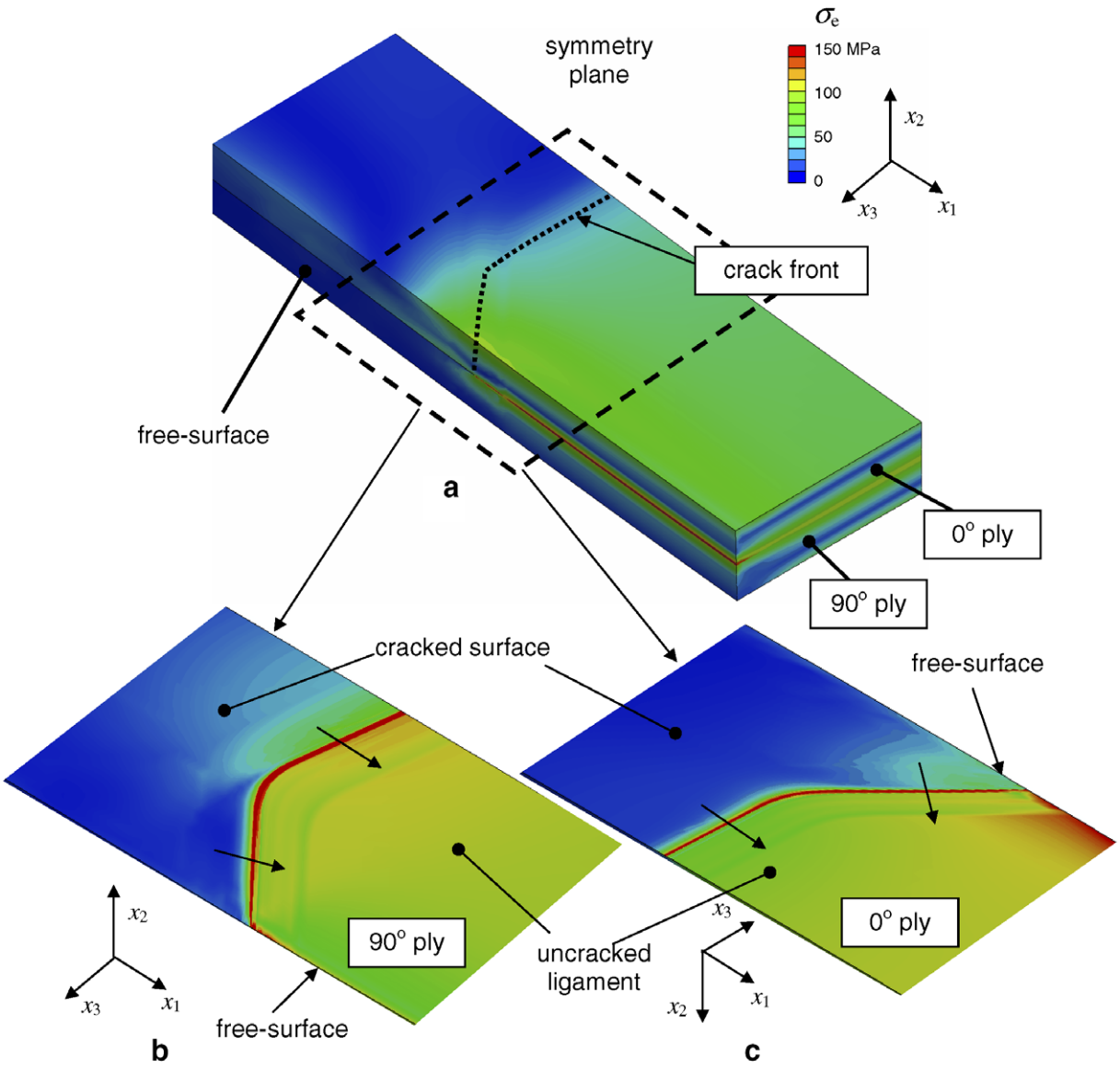

Fig. 8. Shades of effective stress near crack front for $\Delta T = 140$ °C (a) in model *C* showing entire laminate thickness. (b) on 90° side of crack plane and (c) on 0° side of crack plane. Directions of crack growth are also indicated.

$\Delta\mathscr{G}_{th} = 6.9\ \mathrm{J/m^2}$. The observed threshold toughness is more than a magnitude less than the reported interlaminar critical energy release rate for fiber reinforced composites under Mode II condition which typically exceeds $\mathscr{G}_c = 500\ \mathrm{J/m^2}$. These fatigue growth rate results are shown in Fig. 13a, which shows a very good agreement with measured data. Note this fatigue law does not account for the effect of mode mixity. However, since the relative shear mode is nearly constant across the crack fronts as shown in Fig. 12, these parameters should be valid for predominantly shear mode condition. The results are also shown in log–log scale plot in Fig. 13b, which also confirm a good match with the power law model. Additionally, a similar power law model is possible with the stress intensity which yields the exponent as $2m = 0.88$.

In order to evaluate the effect of current unsymmetrical ply arrangement, we also constructed separate 2D models for symmetrical 4 layer models $[0/90]_s$ and $[0/90]_s$ with same geometrical dimensions except for the interface crack. In both models, the pre-cracks were inserted between the 1st and 2nd layers from the top. The computed energy release rate of the $[0/90]_s$ model was 60% of the present unsymmetrical 2 layer model, while for the $[0/90]_s$, it was 69% of the present model. Thus, although the present ply arrangement was chosen to maximize the crack driving force, the energy release or symmetrical specimens are only marginally lower. Furthermore, for the $[0/90]_s$ model, the crack is under (near) Mode I condition. This suggests its threshold fatigue growth resistance to be less than that of Mode II dominant case as in the present unsymmetrical model.

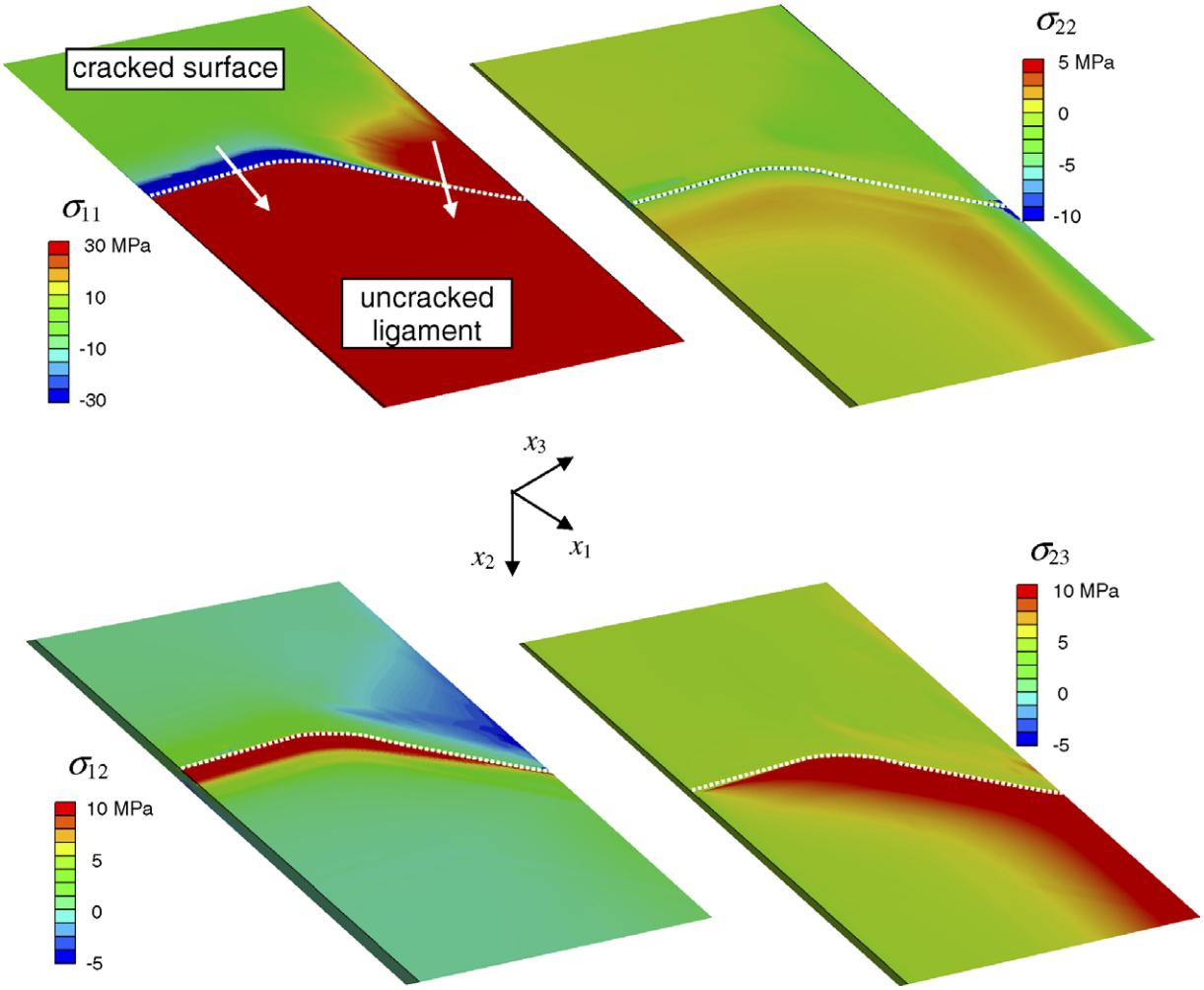

Fig. 9. Shades of various stress components on the 0° ply side of crack plane for model *C* with $\Delta T = 140$ °C. The stress on are also shown.

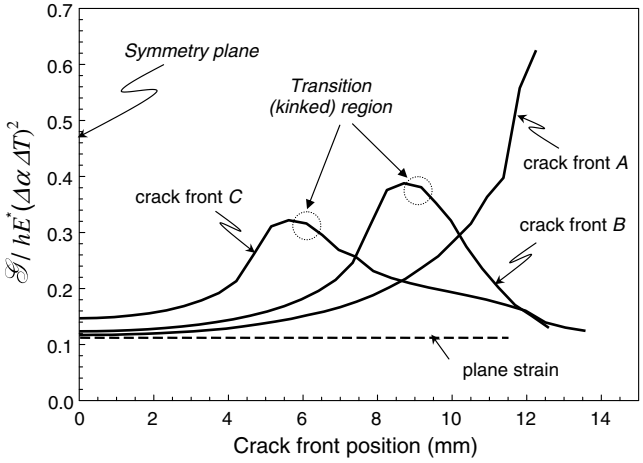

Fig. 10. Normalized $\mathscr{G}$ along crack front for three different models/stages of growth (*A* to *C*).

5. Discussions

In typical cross-ply composite laminates, multi-layered arrangements add larger constraint, and interlaminar crack growth may be more difficult than in the current 2-layer specimen. However, magnitudes of thermal stresses generated by CTE mismatch are still similar. Furthermore, if structures are subjected to mechanical loads as well, the likelihood of fatigue crack growth may increase. In addition, other factors including environmental degradation may promote fatigue crack growth.

In the current study, we fabricated laminate specimens with the vacuum bagging technique so that delamination could be introduced prior to thermal cycling. In practice, delamination may occur due to weak bonding or after repeated mechanical loading and/or under severe environmental conditions. The present tests confirm that such crack can grow under thermal cycles albeit under certain conditions. Examination of the fractured surface revealed complex crack propagation behavior. The path alternated between the 0° and 90° laminae. This was probably due to the dominant Mode II condition but it also confirms that a high bonding strength exists between the plies. This adds an assurance that growth under thermal cycling occurred not because of weak adhesion caused by the present fabrication process, but due to inherent stresses in the laminates.

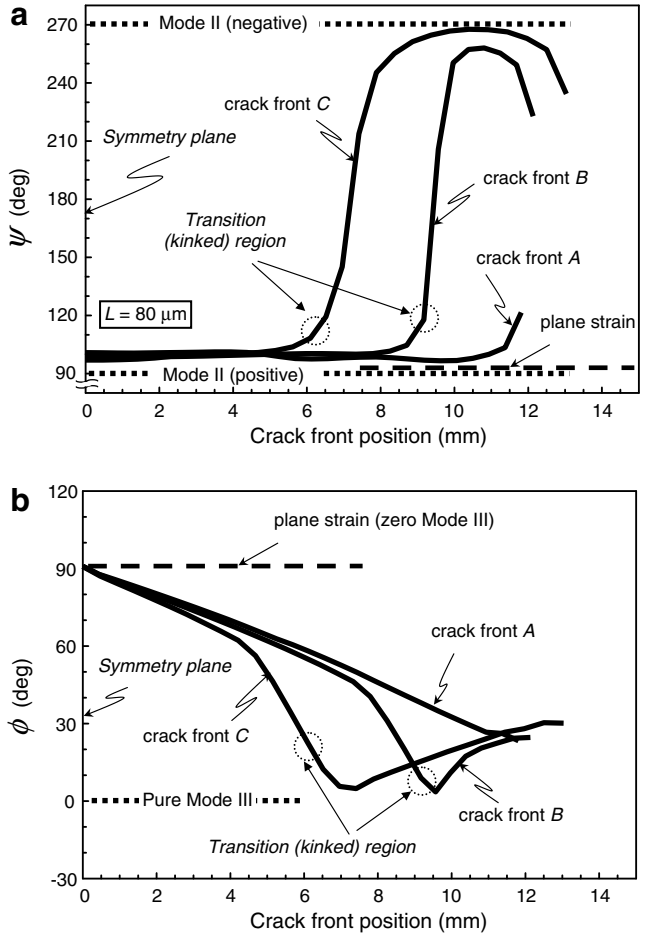

Fig. 11. Phase angle variations along crack front for three different models. (a) In-plane phase angle. (b) Out-of-plane phase angle.

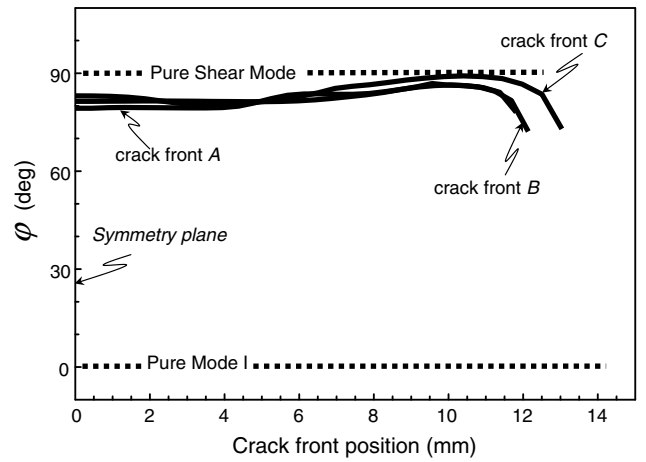

Fig. 12. Effective phase angle variation along crack front for three different models.

Table 1
Energy release rate and corresponding growth rate at different temperatures

ΔT (°C)	$\Delta\mathscr{G}$ (J/m^2)	da/dN (μm/cycle)
3D Interpretation		
30	5.1	0
60	20.6	1.22 ± 0.07
100	57.3	2.69 ± 0.07
120	82.5	3.08 ± 0.07
140	112.0	3.71 ± 0.07
2D Interpretation		
30	2.8	0
60	1.3	1.68 ± 0.07
100	31.5	3.59 ± 0.07
120	45.4	4.25 ± 0.07
140	61.9	5.11 ± 0.07

Interpretations based on 3D and 2D models are made.

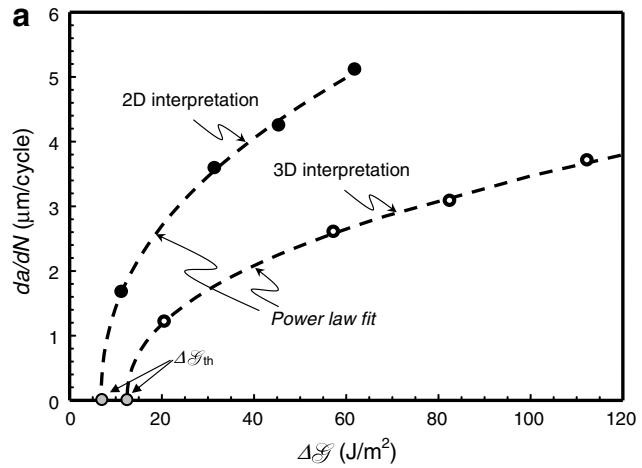

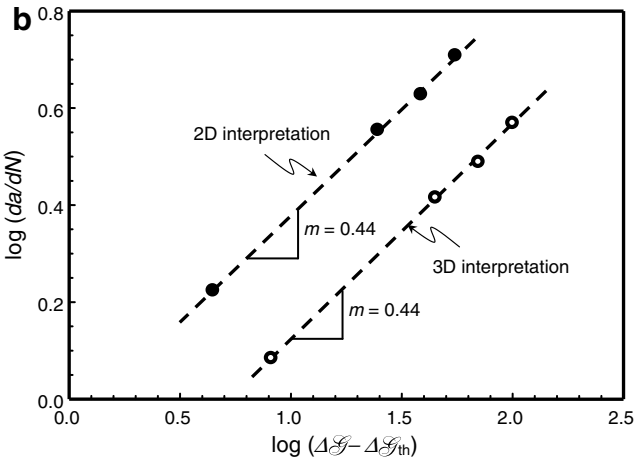

Fig. 13. Measured fatigue crack growth rates shown as function of energy release rate amplitude on (a) regular scales and (b) log–log scales.

The observation of fractured surfaces also revealed uneven crack growth across the width. Analysis of angled crack front from an initially straight front was made with recourse to a 3D finite element model. First the local/point-wise energy release rate value and the two phase angles were computed along the three-dimensional crack front. Next, the crack growth rate was correlated with range of energy release rate using a power law relation. Furthermore, a threshold value of range of energy release rate ($\Delta\mathscr{G}_{th}$) was estimated, below which there was no crack

propagation. Computations show that values for energy release rate are higher for the three-dimensional case as compared to the two-dimensional case for similar thermal loading conditions. Thus a 2D interpretation would offer a conservative estimate for fatigue life of cross-ply laminates submitted to thermal cycling. Nonetheless, while studies on composite laminates might base their investigation on two-dimensional computational analyses for fatigue crack growth characterization, our study reveals that three-dimensional effects play a significant role on the interface crack propagation behavior in such materials.

As noted earlier, Mode I test under monotonic load measured the toughness to be $\mathscr{G}_c = 155\ \mathrm{J/m^2}$ for the present specimen. Although somewhat small, it is within reported values of interlaminar toughness of various carbon fiber-reinforced epoxy laminates ($\mathscr{G}_c = 100$–$1500\ \mathrm{J/m^2}$ [21]). In addition corresponding Mode II values are often 2–3 times higher than those of Mode I [21]. However the estimated value of threshold fatigue crack growth was only $\Delta\mathscr{G}_{th} = 12.5\ \mathrm{J/m^2}$ under Mode II dominant condition. This represents a small fraction of the interlaminar toughness under monotonic load (corresponding threshold temperature is $\Delta T = 47\ ^\circ\mathrm{C}$). Although with a different ply arrangement, a significant drop in the threshold toughness of interlaminar fatigue growth under mechanical load was also observed by Sjogren and Asp [23]. They reported the toughness decrease of $\mathscr{G}_c = 1002\ \mathrm{J/m^2}$ under monotonic load to $\Delta\mathscr{G}_{th} = 100\ \mathrm{J/m^2}$ under cyclic mechanical load for the Mode II case. In addition, threshold values at $T = 100\ ^\circ\mathrm{C}$ were 30–50% lower than those at the room temperature.

We have used an unsymmetrical lay-up to maximize the fatigue growth. As noted in Section 4, more common symmetrical ply arrangements reduce energy release rate by 30–40% for the 4-layer model and probably somewhat more for higher number of layers. Nonetheless, in terms of stress intensity factors, the differences are much less, and under some conditions, a dominant mode can be closer to Mode I. As described above, an interface fatigue crack is likely to grow faster under such a condition (under same $\mathscr{G}$). This implies that even though the threshold temperature for fatigue growth may be higher for symmetrical lay-ups, it may not be always much higher that the values reported here. Thus, the current results should be useful in assessing interlaminar failure resistances of cross-ply laminates subjected to thermal cyclic condition.

Acknowledgements

The authors gratefully acknowledge the US Army Research Office for their support under STTR contract W911NF-06-C-0180 through MesoScribe Technologies, Inc., and also the support of National Science Foundation under the grant CMS-0219250.

References

[1] Vaddadi P, Nakamura T, Singh RP. Transient hygrothermal stresses in fiber reinforced composites: a heterogeneous characterization approach. Compos Part A: Appl Sci Manuf 2003;34(8):719–30.
[2] Azimi HR, Pearson RA, Hertzberg RW. Role of crack tip shielding mechanisms in fatigue of hybrid epoxy composites containing rubber and solid glass spheres. J Appl Polym Sci 1995;58(2):449–63.
[3] Bucknall CB, Dumpleton P. Effects of loading history on fatigue crack growth in high density polyethylene and toughened poly (methyl methacrylate). Polym Eng Sci 1987;27(2):110–5.
[4] Lowe A, Kwon OH, Mai YW. Fatigue and fracture behavior of novel rubber modified epoxy resins. Polymer 1996;37(4):565–72.
[5] Figiel L, Kaminski M. Mechanical and thermal fatigue delamination of curved layered composites. Comput Struct 2003;81(18–19): 1865–73.
[6] Lafarie-Frenot MC, Ho NQ. Influence of free edge intralaminar stresses on damage process in CFRP laminates under thermal cycling conditions. Compos Sci Technol 2006;66(10):1354–65.
[7] Kashtalyan M, Soutis C. Analysis of composite laminates with intra- and interlaminar damage. Prog Aerosp Sci 2005;41(2):152–73.
[8] Eselun SA, Neubert HD, Wolff EG. Microcracking effects on dimensional stability. In: National SAMPE technical conference. In: Proceedings of the 24th conference, 1979. p. 1229–309.
[9] Cohen D, Hyer MW, Tompkins SS. The effects of thermal cycling on matrix cracking and stiffness changes in composite tubes. In: National SAMPE technical conference. In: Proceedings of the 16th conference, 1984. p. 577–88.
[10] Herakovich CT, Hyer MW. Damage-induced property changes in composites subjected to cyclic thermal loading. Eng Fract Mech 1986;25(5–6):779–91.
[11] Adams DS, Bowles DE, Herakovich CT. Thermally induced transverse cracking in graphite/epoxy cross-ply laminates. J Reinf Plast Compos 1986;5(3):152–69.
[12] Kellogg KG, Kallmeyer AR, Dutta PK. Influence of moisture and reduced-temperature thermal cycles on the izod notch toughness of a pultruded glass-fiber composite. Int J Offshore Polar Eng 2003;13(3):232–9.
[13] Dutta PK, Kalafut JF, Lord, HW. Response of advanced composite space materials to thermal cycling. In: Proceedings of the engineering, construction and operations in space, 1988. p. 506–17.
[14] Tang T, Hui CY, Retsos HG, Kramer EJ. Characterization of a fracture specimen for crack growth in epoxy due to thermal fatigue. Eng Fract Mech 2005;72(5):791–805.
[15] Gurumurthy CK, Kramer EJ, Hui CY. Hydro-thermal fatigue of polymer interfaces. Acta Mater 2001;49(16):3309–20.
[16] Paris PC, Gomez MP, Anderson WE. A rational analytic theory of fatigue. Trend Eng 1961;13(1):9–14.
[17] Vaddadi P, Nakamura T, Singh RP. Inverse analysis to determine hygrothermal properties in fiber reinforced composites. J Compos Mater 2007;41:309–34.
[18] Heyder M, Kuhn G. 3D fatigue crack propagation: experimental studies. Int J Fatigue 2006;28(5–6):627–34.
[19] Nakamura T, Kushner A, Lo CY. Interlaminar dynamic crack propagation. Int J Solids Struct 1995;32(17):2657–75.
[20] Yang W, Suo Z, Shih CF. Mechanics of dynamic debonding. Proc Royal Soc A 1991;433:679–97.
[21] Daniel IM, Ishai O. Engineering mechanics of composite materials. Oxford University Press; 1994.
[22] Nakamura T, Parks DM. Anti-symmetrical 3D stress field near the crack front of a thin elastic plate. Int J Solids Struct 1989;25:1411–26.
[23] Sjogren A, Asp LE. Effects of temperature on delamination growth in carbon/epoxy composite under fatigue loading. Int J Fatigue 2002;24:179–84.